J. Fluid Mech. (2017), *vol.* 813, *pp.* 85–109.
doi:10.1017/jfm.2016.829

Flow regimes for a square cross-section cylinder in oscillatory flow

Feifei Tong[1,†], Liang Cheng[1,2], Chengwang Xiong[1], Scott Draper[1,3], Hongwei An[1] and Xiaofan Lou[1]

[1]School of Civil, Environmental and Mining Engineering, The University of Western Australia, 35 Stirling Highway, Perth, WA 6009, Australia

[2]State Key Laboratory of Coastal and Offshore Engineering, Dalian University of Technology, Dalian, 116024, China

[3]Centre of Offshore Foundation System, The University of Western Australia, 35 Stirling Highway, Perth, WA 6009, Australia

(Received 2 May 2016; revised 24 November 2016; accepted 5 December 2016; first published online 17 January 2017)

Two-dimensional direct numerical simulation and Floquet stability analysis have been performed at moderate Keulegan–Carpenter number (KC) and low Reynolds number (Re) for a square cross-section cylinder with its face normal to the oscillatory flow. Based on the numerical simulations a map of flow regimes is formed and compared to the map of flow around an oscillating circular cylinder by Tatsuno & Bearman (*J. Fluid Mech.*, vol. 211, 1990, pp. 157–182). Two new flow regimes have been observed, namely A′ and F′. The regime A′ found at low KC is characterised by the transverse convection of fluid particles perpendicular to the motion; and the regime F′ found at high KC shows a quasi-periodic feature with a well-defined secondary period, which is larger than the oscillation period. The Floquet analysis demonstrates that when the two-dimensional flow breaks the reflection symmetry about the axis of oscillation, the quasi-periodic instability and the synchronous instability with the imposed oscillation occur alternately for the square cylinder along the curve of marginal stability. This alternate pattern in instabilities leads to four distinct flow regimes. When compared to the vortex shedding in otherwise unidirectional flow, the two quasi-periodic flow regimes are observed when the oscillation frequency is close to the Strouhal frequency (or to half of it). Both the flow regimes and marginal stability curve shift in the (Re, KC)-space compared to the oscillatory flow around a circular cylinder and this shift appears to be consistent with the change in vortex formation time associated with the lower Strouhal frequency of the square cylinder.

Key words: instability, low-Reynolds-number flows, vortex flows

1. Introduction

Oscillatory flow around a square cylinder has been the subject of a number of studies (Bearman *et al.* 1985; Venugopal, Varyani & Barltrop 2006), although it is not as extensively explored as its circular cylinder counterpart. The sharp

†Email address for correspondence: feifei.tong@uwa.edu.au

corners distinguish it from flow around smooth-edged bluff bodies, in that they constrain the locations of flow separation. One of the seminal studies on oscillatory sharp-edged bluff bodies was carried out by Keulegan & Carpenter (1958), who discovered the correlation between drag (C_D) and inertia (C_M) coefficients with the Keulegan–Carpenter number (KC), which is also called the period number and is defined as,

$$KC = \frac{U_m T}{D} = \frac{2\pi A}{D}, \tag{1.1}$$

where D is the characteristic length of the bluff body (i.e. edge length of a square); U_m and T are the amplitude and period of the velocity oscillation, respectively; and A is the amplitude of fluid particle excursions. An oscillatory Reynolds number (Re) can be defined as,

$$Re = \frac{U_m D}{\nu} = \frac{2\pi A D}{T\nu}, \tag{1.2}$$

where ν is the kinematic viscosity of the fluid. The ratio of Re to KC is known as the frequency parameter or Stokes number (β), so that

$$\beta = \frac{Re}{KC} = \frac{D^2}{\nu T}. \tag{1.3}$$

Investigations on oscillatory flow around sharp-edged structures have been motivated largely by engineering applications, of which wave forces on structures provide a well-known example. Theoretical efforts were made by Graham (1980), who presented an analysis of the forces induced by oscillatory flow on sharp-edged cylinders at relatively low KC and high Re, with the drag coefficient being expressed as a function of KC and the internal angle (α) of the sharp corner. Bearman *et al.* (1985) compared the in-line forces between theoretical and experimental results for a square-section cylinder with its face aligned normal (0°) or 45° to the incoming flow. The inviscid theory was found to be valid for $KC < 3$ and the prediction on the inertia coefficient is more reasonable for the square cylinder than for the diamond cylinder. By assuming a laminar, non-separating flow condition Troesch & Kim (1991) built a theoretical model based on experimental tests valid for a variety of shapes including squares, however the model is only adequate for KC close to zero. Bearman *et al.* (1984) measured the effect of corner radius on the in-line forces in a parameter space of $1 \leqslant KC \leqslant 100$ and $200 \leqslant Re \leqslant 2 \times 10^4$. It was found that the variation of drag coefficient with KC behaves very differently from that of a circular cylinder and the drag coefficient is more sensitive to corner radius in oscillatory flow than in steady flow. It was suggested that flow separation around sharp-edged structures is responsible for the drag characteristics. Similarly, Venugopal *et al.* (2006) observed that the sharp edges play a significant role in flow separation and vortex shedding around submerged rectangular cylinders under both regular and random free-surface waves. They concluded that sharp edges lead to the relatively large values of drag coefficients at low KC compared to that observed for a circular cylinder (at $KC < 5$ and $Re \cong 10^3$–10^5). Meanwhile, the inertia coefficient was observed to drop as much as 50 % with the increase of KC. Barrero-Gil (2011) experimentally investigated in-line forces of a square cylinder at $KC < 15$ and $\beta = 29$ and 40 ($Re < 600$). They found the drag coefficient evolves with KC in a similar way to that of a circular cylinder but at a higher value, while the inertia coefficient shows much less dependence on KC.

Numerical studies on the subject are less common, with the majority based on two-dimensional (2-D) models. Smith & Stansby (1991) and Zheng & Dalton (1999),

Researchers	KC	Re	Method	Alignment
Bearman *et al.* (1984)	1–100	200–2×10^4	Experimental	0°/45°
Bearman *et al.* (1985)	<10	<4130	Experimental	0°/45°
Troesch & Kim (1991)	0.079–0.58	1.8×10^3–2.5×10^4	Experimental	0°
Smith & Stansby (1991)	⩽3	⩽864	Numerical	0°/45°
Zheng & Dalton (1999)	1–5	<2160	Numerical	0°/45°
Venugopal *et al.* (2006)	0–5	6.397×10^3–1.18×10^5	Experimental	0°
Chern *et al.* (2007)	1–15	200–500	Numerical	0°
Barrero-Gil (2011)	2–15	80–600	Experimental	0°

TABLE 1. Selected studies on a square cylinder in oscillatory flow.

for example, carried out 2-D numerical studies of rectangular cylinders in oscillatory flow at low KC number ($\leqslant 5$). Both studies focused on the force coefficients with brief discussions on the flow features to interpret their results. Chern *et al.* (2007) numerically studied the force coefficients and the flow field for a square cylinder in oscillatory flow at Re between 200–500 and $KC \leqslant 15$. They concluded, in agreement with Venugopal *et al.* (2006), that Re only has very limited effect on the measured drag and inertia coefficients.

Summarised in table 1, the aforementioned studies were mainly concerned with hydrodynamic forces on the sharp-edged structure induced by the flow. However, little attention has been devoted to the flow regimes around this type of structure. On the contrary, oscillatory flow around a circular cylinder has been the subject of sustained research over the last few decades (Bearman *et al.* 1985; Williamson 1985; Tatsuno & Bearman 1990; Sarpkaya 2002; Elston, Blackburn & Sheridan 2006). The aspects covered in those studies range from hydrodynamic forces to flow phenomena. Comprehensive flow regimes were firstly identified by Williamson (1985) and then by Tatsuno & Bearman (1990) in more detail. Unlike the flow field near the onset of instability around a circular cylinder in uniform flow (Williamson 1996), there is an intriguing set of 2-D and three-dimensional (3-D) instabilities when it is placed in sinusoidal oscillating flow.

Williamson (1985) investigated the cross-sectional flow regimes at $\beta = 255$ ($Re < 1.53 \times 10^4$) for a circular cylinder and found that the vortices from a previous oscillation half-cycle interact with those formed in the present half-cycle, leading to several repeatable flow regimes. The vortex-shedding regimes were classified based on the number of vortex pairs generated per motion cycle. These include a pairing regime of attached vortices at $KC < 7$; a transverse vortex street regime at $7 < KC < 13$; a single-pair regime of vortices at $13 < KC < 15$; a double-pair regime at $15 < KC < 24$; a three-pair regime at $24 < KC < 32$; and a four-pair regime for $32 < KC < 40$.

Shortly later, Tatsuno & Bearman (1990) identified eight regimes of remarkable flow patterns at a lower range of KC(<15) and β (<160, i.e. $Re \lesssim 1200$) through detailed flow visualisation in the cross-sectional plane and along the axis of the cylinder. Within these eight regimes, regimes A* and A represent flows that are 2-D and symmetric to the direction of motion, with vortex shedding occurring in regime A but not in A*. Regime B features the so-called 'streaked flow' along the axis of the circular cylinder, which is comprised of equally spaced streaks of mushroom-shape flow structure (Honji 1981). An, Cheng & Zhao (2011) demonstrated through numerical simulations that the spacing between Honji vortices show strong correlations with KC over $50 \leqslant \beta \leqslant 500$. A key observation in regime C is that

the vortex shedding does not synchronise with the imposed oscillation; rather it is rearranged into larger vortices over a secondary period before emanating in the directions of motion. The transverse vortex streets are found in regimes D and E, where vortices are convected obliquely to one side of the axis of oscillation. Irregular switching of the convection direction is observed in regime E. Diagonal double-pair vortices feature in regime F. The last flow regime is regime G, which breaks the cross-sectional and spanwise symmetries and thus is chaotic and irregular. Flows in regimes B, D and F are all 3-D with a well-defined spatial periodicity in the spanwise direction, with the spanwise wavelength ranging from approximately one diameter (in regime B) to six diameters (in regime F). Regimes A, D, E and F are synchronous regimes, since the vortex shedding is synchronised with the oscillation. Except regime B, where the cross-sectional flow field at most locations resembles regime A*, subsequent 2-D numerical studies (Justesen 1991; Nehari, Armenio & Ballio 2004; Elston *et al.* 2006) have reproduced much of the cross-sectional flow feature in these eight regimes. This demonstrates that the three-dimensionality is weak and the cross-sectional vortex streets are induced by 2-D instabilities rather than 3-D instabilities.

Elston *et al.* (2006) studied the 2-D and 3-D symmetry-breaking instabilities of flows around a circular cylinder at $KC \leqslant 10$ and $\beta \leqslant 100$ ($Re < 1000$) through Floquet analysis and direct numerical simulation. Flow regimes between A–C, A–D, A*–B and B–E were investigated in the KC and β parameter space. It was found from 2-D Floquet analysis that the instability is synchronous with the forcing at low β but becomes quasi-periodic with a well-defined secondary period at high β, resulting in distinct flow modes. In addition, at $\beta < 50$, the flow is almost immediately unstable to 3-D secondary instabilities as soon as 2-D primary stability is broken, with the two marginal curves collapsing together. For $\beta > 50$, however, a direct primary breakage was found, where with the increase of KC, the flow is unstable to 3-D instability before it breaks 2-D instability, and both of these two bifurcations are found to be supercritical.

These flow regimes are not necessarily restricted to circular cylinders, and recent research has revealed that they can appear around multiple bluff bodies (Zhao & Cheng 2014; Tong *et al.* 2015), elliptical foils (Deng & Caulfield 2016) as well as a circular cylinder undergoing combined oscillatory rotation and translation (Koehler *et al.* 2015). Not surprisingly, the locations of these regimes in terms of KC and β are dependent on the parameters defining these scenarios.

It is worthwhile noting that in the majority of the previous studies on bluff bodies immersed in oscillatory flow, β, rather than Re, has been used as an independent parameter, along with KC. This is partially due to the classical analyses on inertia and drag forces by Stokes (1851) and Wang (1968) at $KC \ll 1$, where the force can be expressed in the form of a power expansion of $\beta^{-1/2}$. On the other hand, at high Re and moderate KC, Sarpkaya (1976) found that β is important in describing the force behaviour as well as vortex-shedding frequencies for a circular cylinder. Despite this, Re is used as an independent parameter with KC here. The motivation is that both the oscillation amplitude and frequency, as represented by Re in (1.2), are key parameters that define the flow regime at low $Re(\leqslant 200)$ and moderate $KC(\leqslant 15)$. It should be noted, however, that either β or Re can be easily reconstructed from each other.

The present work investigates oscillatory flow around a square cylinder via 2-D direct numerical simulations and Floquet analysis in a parameter space of $KC \leqslant 15$ and $Re \leqslant 200$. The primary objective is to identify and explain various flow regimes. The 2-D numerical simulation is justified since the three-dimensionality is relatively

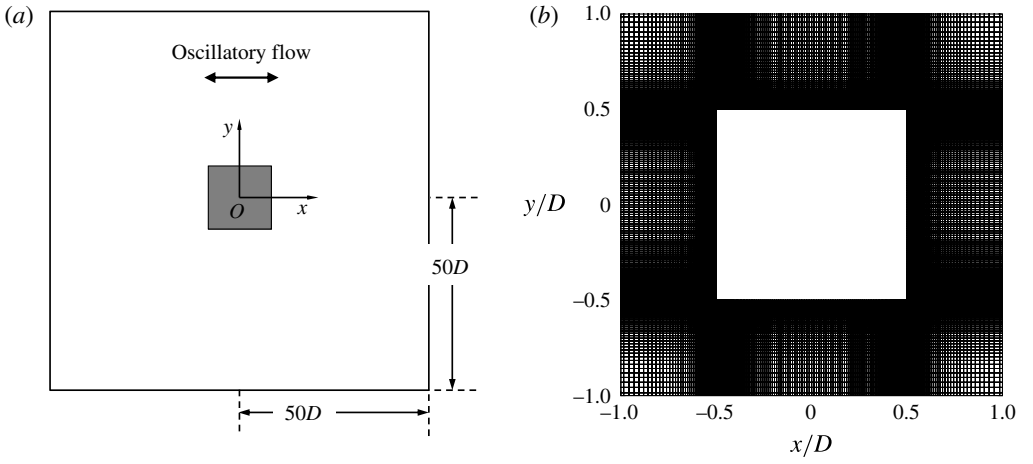

FIGURE 1. Schematic representation of the problem investigated in the present paper, (*a*); and mesh distribution around the square cylinder in the direct numerical simulation, (*b*). The coordinate system is defined in (*a*), where the spanwise direction, z-axis, is normal to the (x, y)-plane.

weak in the selected parameter space. In addition, the transition between different flow regimes discovered by Tatsuno & Bearman (1990) is largely induced by 2-D instability (except regime B). It is acknowledged, however, that the map of flow regime obtained using 2-D simulations may differ from those produced by 3-D simulations, in a similar way to that observed for a circular cylinder (Elston *et al.* 2006). The remainder of the paper is organised in the following manner. In § 2, the governing equations, numerical models and model validations are introduced. Section 3 presents the classification of the flow regimes and proposes a correlation for the occurrence of the flow regimes with that in unidirectional flow. The major conclusions are drawn in § 4.

2. Methodology

2.1. *Flow regime classification*

As illustrated in figure 1(*a*), this paper investigates the flow regime formed around a stationary-square cross-section cylinder immersed in oscillatory flow under small KC and Re conditions. The flow regime classification is based on the nomenclature of Tatsuno & Bearman (1990) and the 2-D symmetry criteria used by Nehari *et al.* (2004) and Elston *et al.* (2006). The symmetry breaking in the 2-D numerical simulations is visually identified by observing the non-dimensional vorticity field which is defined as,

$$\omega_z = \nabla \times \boldsymbol{U}(D/U_m), \tag{2.1}$$

where $\boldsymbol{U}$ is the velocity vector with velocity components u_x and u_y in the x- and y-directions, respectively. The symmetry states, defined by Elston *et al.* (2006), are listed below for convenience:

$$y\text{-reflection}, \quad K_y : \omega_z(x, y, t) = -\omega_z(x, -y, t), \tag{2.2}$$

$$\text{spatio-temporal}, \quad H_1 : \omega_z(x, y, t) = -\omega_z(-x, y, t + T/2), \tag{2.3}$$

$$\text{spatio-temporal}, \quad H_2 : \omega_z(x, y, t) = \omega_z(-x, -y, t + T/2). \tag{2.4}$$

To consider the temporal behaviour, flow streaklines are generated by releasing massless fluid particles from the body. The particles are released after the simulations become fully established, generally after $t = 90T$.

2.2. *Direct numerical simulation model*

The flow fields have been simulated using direct numerical simulation (DNS), which directly solves the Navier–Stokes (NS) equations without turbulence models. The vector form of incompressible NS equations are expressed as,

$$\boldsymbol{\nabla} \cdot \boldsymbol{U} = 0, \tag{2.5}$$

$$\frac{\partial \boldsymbol{U}}{\partial t} + (\boldsymbol{U} \cdot \boldsymbol{\nabla})\boldsymbol{U} = -\frac{1}{\rho}\boldsymbol{\nabla} p + \nu \nabla^2 \boldsymbol{U}, \tag{2.6}$$

where t is time, ρ is the density of the fluid and p is pressure. The above equations are solved in two dimensions using the open source field operation and manipulation (OpenFOAM®) C++ libraries. The finite volume method is used and pressure–velocity coupling is achieved following the pressure implicit with splitting of operators (PISO) method. The convection terms are discretised using the Gauss cubic scheme, while the Laplacian and pressure terms in the momentum equations are discretised using the Gauss linear scheme. The Euler implicit scheme is used for temporal discretisation.

A square computational domain is employed in the DNS study as shown in figure 1(*a*), with the cylinder being placed at the centre. Unless otherwise specified, the initial values of flow velocity and pressure are set to zero in the domain. Flow velocity and pressure boundary conditions on the left boundary are given as

$$u_x(t) = U_m \sin(2\pi f_o t), \tag{2.7}$$

$$\frac{\partial p(t)}{\partial x} = U_m 2\pi f_o \cos(2\pi f_o t), \tag{2.8}$$

where f_o is the oscillation frequency ($=1/T$). At the right boundary, the velocity gradients in the x-direction and the pressure are set to zero. The free-slip flow condition is used at the two lateral boundaries that are parallel to the flow directions. A no-slip condition is applied on the body, where the velocity and normal pressure gradient are set to zero.

The computational domain size and mesh employed in the DNS study were chosen based on previous experience with modelling oscillatory flow around circular cylinders over a similar parameter space (Tong *et al.* 2015), following refinement based on a mesh dependence check. The length of the chosen square domain is $100D$, leading to a blockage ratio of 1 %. As shown in figure 1(*b*), a structured mesh that has a similar mesh density to Mesh 4 in Tong *et al.* (2015) is employed. The smallest mesh size in the face-normal direction of the cylinder is $0.003D$. The number of mesh elements on each face of the square cylinder is 120, resulting in 480 elements surrounding the body. This is three times that used for the circular cylinder due to a need to refine the mesh around the sharp corners. Since the present DNS model is well validated, only validation on drag (C_D) and inertia (C_M) coefficients of the square cylinder are presented in figure 2. The force coefficients are calculated from the Morison equation:

$$F_x = \frac{1}{2}\rho D C_D |u_x(t)| u_x(t) + \rho D^2 C_M \frac{\mathrm{d}u_x(t)}{\mathrm{d}t}, \tag{2.9}$$

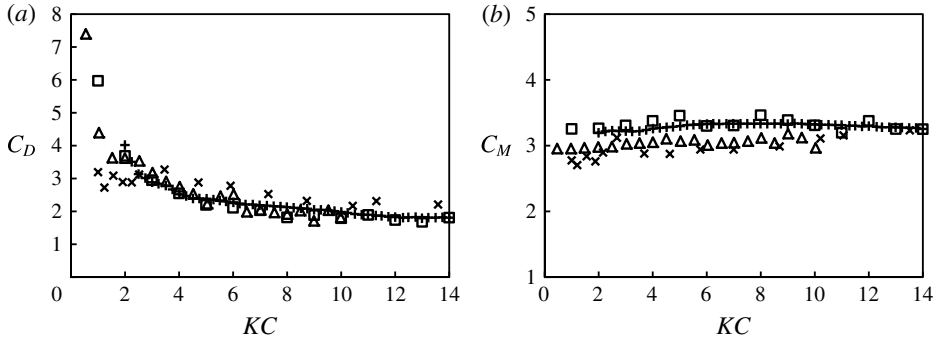

FIGURE 2. Comparison of the drag (C_D) and inertia (C_M) coefficients by the present DNS method at $\beta = 40$ (□) with experimental data by Barrero-Gil (2011) at $\beta \approx 40$ (+) and Bearman *et al.* (1984) at $\beta = 213$ (×), and with numeric values computed by Scolan & Faltinsen (1994) at $\beta = 213$ (△).

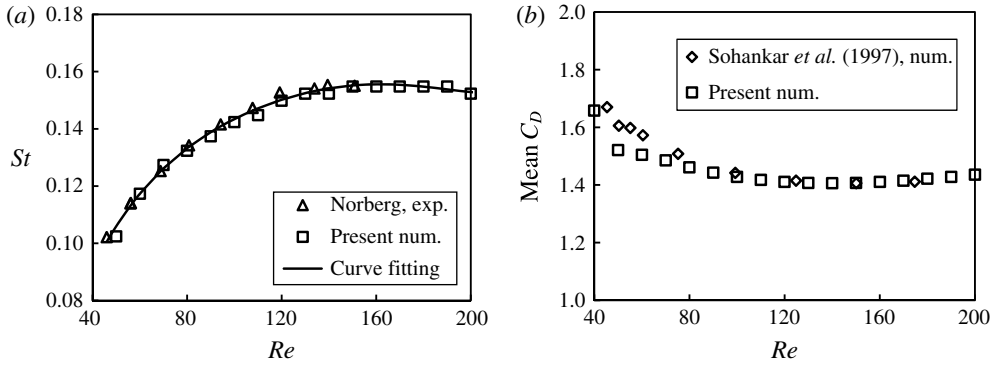

FIGURE 3. Comparison of (*a*) the vortex-shedding frequency (*St*) and (*b*) mean drag coefficient (C_D) of a square cylinder in steady flow at various Reynolds numbers (*Re*); experimental data of Norberg were taken from the numerical study by Sohankar, Norberg & Davidson (1997).

where F_x is the force on the cylinder in the in-line direction and is obtained by integrating the pressure and shear stress along the body. This validation is undertaken at $\beta = 40$ and the forces are compared to experimental data (Bearman *et al.* 1984; Barrero-Gil 2011) and numerical results by Scolan & Faltinsen (1994). It can be seen that good agreement was generally achieved, even at larger *KC* values (>5) where the flows in the experiments are believed to be weakly three-dimensional.

The model is also validated under the condition of steady current at low *Re*. The Strouhal number (*St*) in steady flow is defined as,

$$St = \frac{f_{vs} D}{U_\infty}, \tag{2.10}$$

where f_{vs} and U_∞ are the vortex-shedding frequency and the free-stream flow velocity, respectively. We compare *St* and the mean C_D over $Re = 40$–200 with an interval of 10 with published data in figure 3, anticipating that the results from steady flow will be utilised in interpreting the results for its oscillatory counterpart. Very good agreement

is achieved. Vortex shedding is found at $Re = 50$ and onwards, and the St increases in line with Re for $Re \leqslant 160$. A decline is found in the mean C_D when the vortex shedding starts, and the drop trend continues gradually until approximately $Re = 160$. The drag increases slightly with Re for $Re > 160$.

2.3. *Floquet stability analysis*

Floquet linear stability analysis is also carried out in this study to determine the marginal curve of stability for the 2-D flow in breaking reflection symmetry about the axis of oscillation. An open source spectral element code, Nektar++ (Cantwell *et al.* 2015) is employed for this purpose. The linear stability analysis examines the evolution of an infinitesimal perturbation, $\boldsymbol{u}'(x, y, t)$, over a T-periodic base flow, $\boldsymbol{U}(x, y, t)$, from cycle to cycle by computing the Navier–Stokes equations linearised to $\boldsymbol{U}$ and $\boldsymbol{u}'$ (Barkley & Henderson 1996). Solution of the perturbation can be decomposed into a sum of components $\boldsymbol{u}'(x, y, t) = \tilde{\boldsymbol{u}}(x, y, t)\exp(\sigma t)$. Here, the Floquet eigenfunction $\tilde{\boldsymbol{u}}(x, y, t)$ also holds T-periodicity; and the Floquet exponents σ are complex numbers. One usually looks at the Floquet multiplier to determine the stability state, which is expressed as $\mu \equiv \exp(\sigma T)$. When the Floquet multiplier leaves the unit circle, $|\mu| > 1$ (perturbation grows exponentially), the base flow $\boldsymbol{U}$ is deemed to be unstable to the perturbation, thus instability occurs (Barkley & Henderson 1996); while stability is signalled when the multiplier is inside the unit circle, $|\mu| < 1$ (perturbation decays exponentially). A convergence test for the code is provided in the Appendix.

3. Results discussion

Direct numerical simulations for oscillatory flow around a square cylinder were performed over a parameter space of $KC \in [1, 15]$ and $Re \in [40, 200]$. Initially, the increments of KC and Re in DNS study were set to be 1 and 20, respectively, but these were then refined in regions where a better insight into the detailed characteristics of the flow was needed. The Floquet stability analysis was carried out where the refection symmetry in (2.2) is observed to be broken from DNS results, in order to capture the critical point of transition.

3.1. *Flow regimes*

Flow fields corresponding to selected parameters are visualised through streaklines in figure 4. The streaklines have been generated by releasing 100 massless particles evenly distributed on the body surface, at a frequency of eight times the oscillation frequency. At low Re values the flow possesses a reflection symmetry to the axis of motion (K_y symmetry (2.2)). At large Re values, irregular streaklines are observed, especially in the far field away from the cylinder. Moreover, at intermediate Re values the flow shows a wide range of organised wake features, which lead to distinct spatio-temporal symmetries and quasi-periodic states.

These flow features, together with the vorticity field (spatial behaviour) and the force histories (temporal behaviour), are considered in mapping out the flow regimes shown in figure 5(*a*). The curve of marginal stability from 2-D Floquet stability analysis is also included, which will be detailed in § 3.2. The flow regimes in this figure share similarities to those observed for a circular cylinder in figure 5(*b*) reproduced from Tatsuno & Bearman (1990). Despite this, it should be noted that there are fundamental differences between the two maps of flow regimes. As pointed out by Elston *et al.* (2006), the former is the map of flow modes from 2-D simulations, which represent the cross-sectional subspace as opposed to the later

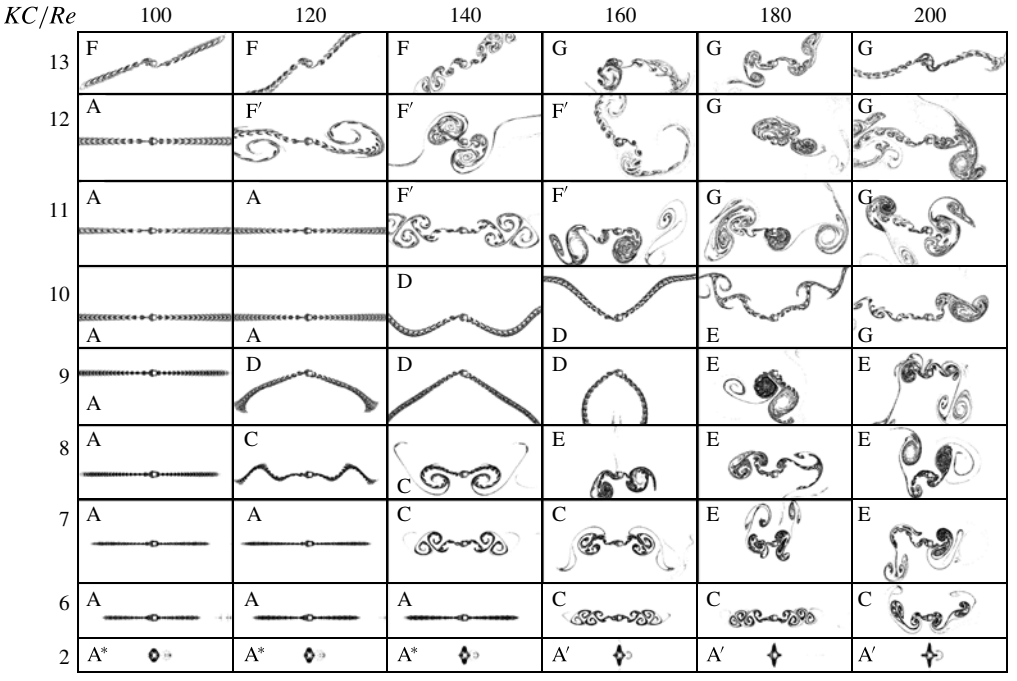

FIGURE 4. Flow fields represented by the streaklines at various *Re* and *KC* conditions. Streaklines were generated by releasing 100 massless particles evenly distributed on the body, at a frequency eight times the oscillatory frequency. The inlet oscillatory flow is in the horizontal direction.

where some are three-dimensional. The 2-D flow regimes are only accurate when the three-dimensionality is weak.

It is seen that the region occupied by regime C in the parameter space is considerably larger than that for the circular cylinder. In contrast, the area occupied by regime D for the square cylinder is relatively small. Due to the sharp corners, flow separation can be observed even at low *KC* and *Re* for the square cylinder, though the separated vortices are not able to travel far. Therefore, no attempt has been made to define the boundary between A and A*. For many cases, the streakline patterns associated with regime G are similar to regime F local to the cylinder, but intermittent switching of convection direction was observed for regime G, as seen in figure 4 at $(Re, KC) = (200, 11 \text{ and } 12)$. The two new flow regimes identified around the square cross-section cylinder, namely regime A′ and F′, will now be mainly focused on.

3.1.1. *Regime A′*

At low *KC* but high *Re* number, a flow regime has been observed for the square cylinder which possesses K_y symmetry in (2.2). The massless particles released in the flow field are mainly convected in the direction perpendicular to the velocity oscillation direction (see figure 4). Figure 6 shows the vortices are mostly attached to the body during the oscillation period. The vortices aligned with the leading edges occupy much larger region than those extended in the oscillation direction. This flow pattern is classified as regime A′ to distinguish it from the regime A*, where massless particles are convected away from the cylinder in the direction of flow oscillation.

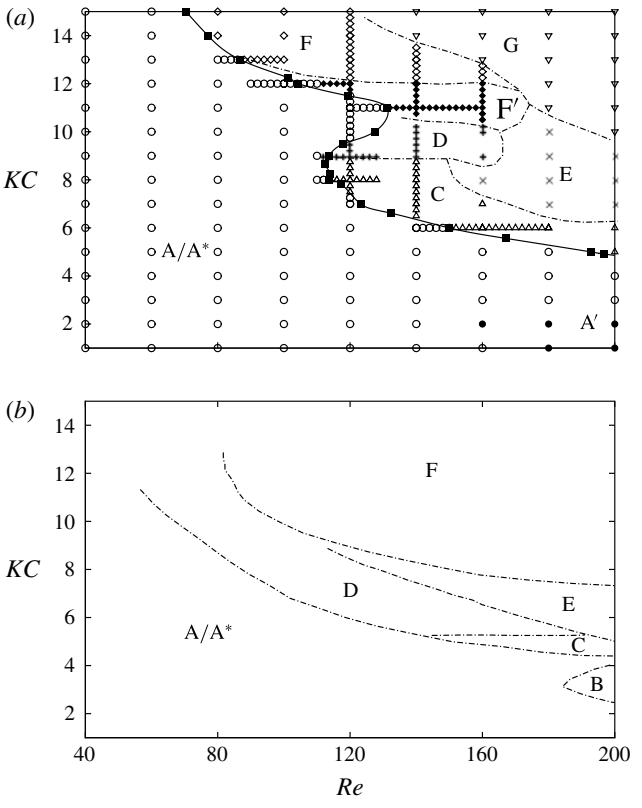

FIGURE 5. Classification of flow regimes for a square cylinder in oscillatory flow based on 2-D DNS and Floquet analysis, (*a*), along with the map of the flow for a circular cylinder (Tatsuno & Bearman 1990) for ease of comparison, (*b*). In (*a*), ○, regimes A/A*; ●, regime A′; △, regime C; +, regime D; ◆, regime F′; ◇, regime F; × regimes E; ▽, regime G; solid lines with ■, marginal stability curve from 2-D Floquet stability analysis of the square cylinder; dash-dotted lines, interpolated boundary lines for different flow regimes. In (*b*), symbols represent flow regimes.

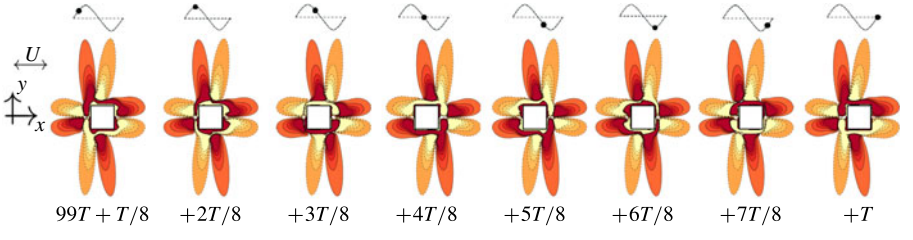

FIGURE 6. (Colour online) Flow regime A′ at (*Re*, *KC*) = (200, 2) as illustrated by vorticity contour between $\omega_z = -0.5$ (light colours) and +0.5 (dark ones) with cutoff level ±0.1. The inlet oscillatory flow is in the horizontal (*x*-axis) direction and the instantaneous time is shown as ● in the sinusoidal velocity signal.

Okajima (1982) demonstrated that at $Re = 150$ and 250 in steady flow, the flow detaches itself from the leading edge of a square cylinder and rolls up behind the cylinder. The separated flow can only reattach to the side surfaces when the aspect ratio extends to 2 (side length to height), where the flow moves along the surfaces,

instead of rolling up into the wake. In regime A′ the shear layers generated from the leading edges are allowed neither to fully reattach to the body due to the short side ratio, nor to travel far from the body due to the short oscillation period. Therefore, when the flow reverses, the shear layer is pushed outwards, feeding a vortex aligned with the leading edge. This gives rise to the released particles moving away from the cylinder in a direction perpendicularly to the oscillation direction.

Regime A′ is only found at $KC = 1$ and 2, and at $Re \gtrsim 160$. This is because at larger KC, the shear layers can travel beyond the ends of the cylinder, while at smaller Re the shear layer is not strong enough to detach from the surface. DNS simulations were carried out in seeking regime A′ for a circular cylinder at $(Re, KC) = (200 - 240, 2)$ without success, where the attached vortices mainly extend in the oscillation direction. In fact experiments were carried out until $Re \sim 300$ at $KC = 2$ by Tatsuno & Bearman (1990), and the released dye/aluminium dust were seen travelling in the oscillation direction.

3.1.2. *Regime F′*

Another new flow regime is observed at high values of KC and intermediate Re, just before regime F appears (for instance, at $KC = 11$, between $Re = 126$–160, and at $Re = 140$, between $KC = 10.75$–12). This flow is quasi-periodic (QP), which can be seen in figure 4 at $(Re, KC) = (140, 11$ and $12)$ and $(120, 12)$. This regime is classified as F′ and is distinct from regime F because the shed vortices do not synchronise with the motion. Instead, they are rearranged into large vortex cores with a well-defined secondary period. Regime F′ differs from regime C in terms of the convection directions of the shed vortices.

Detailed features typical to regime F′ are illustrated in figure 7 for $(Re, KC) = (140, 11)$. It can be seen that a low secondary frequency (f_s) exists in the lift force, and this frequency modulates the main frequency at $f/f_o = 1$ (where frequency of lift force, f, is non-dimensionalised by flow oscillation frequency $f_o = 1/T$), resulting in two peaks at 0.94 and 1.12. This suggests that the secondary period is approximately 11 times the flow oscillation period. This is consistent with figure 7(*c*), where vortices of the same sign merge with each other to form a larger vortex, whose sign switches approximately every $5.5T$. For instance, vortex I at $t/T = 86$ is replaced by vortex I′ at $t/T = 91$. The shed vortices emanate in inclined diagonal directions, rather than in the flow direction as observed in regime C (figure 8*a*). Regime F′, along with the secondary period, are believed to be induced by the modulation between oscillation and vortex formation frequencies, which is explained in § 3.3.

Figures 8 and 9 compare regime F′ with F and another QP state regime C. This comparison is presented in terms of the flow field, the time history of lift coefficient C_L, the FFT spectrum of C_L and Lissajous plots of C_L against in-line force coefficient C_I. Here, C_L and C_I are defined as,

$$C_L = \frac{F_y}{0.5\rho D U_m^2}, \quad C_I = \frac{F_x}{0.5\rho D U_m^2}. \tag{3.1a,b}$$

It is obvious that regime F′ is similar to regime C, in the sense of their quasi-periodicity. Unlike the Lissajous plots of regime F, which almost collapses into a single line, C_L of regime F′ and regime C show a periodicity over many periods of harmonic motion. This is further evidenced by the frequency spectra, where a modulation to the oscillation frequency is clear. A low non-dimensional frequency of 0.07 is detected at $(Re, KC) = (160, 7)$ for regime C, which modulates the main

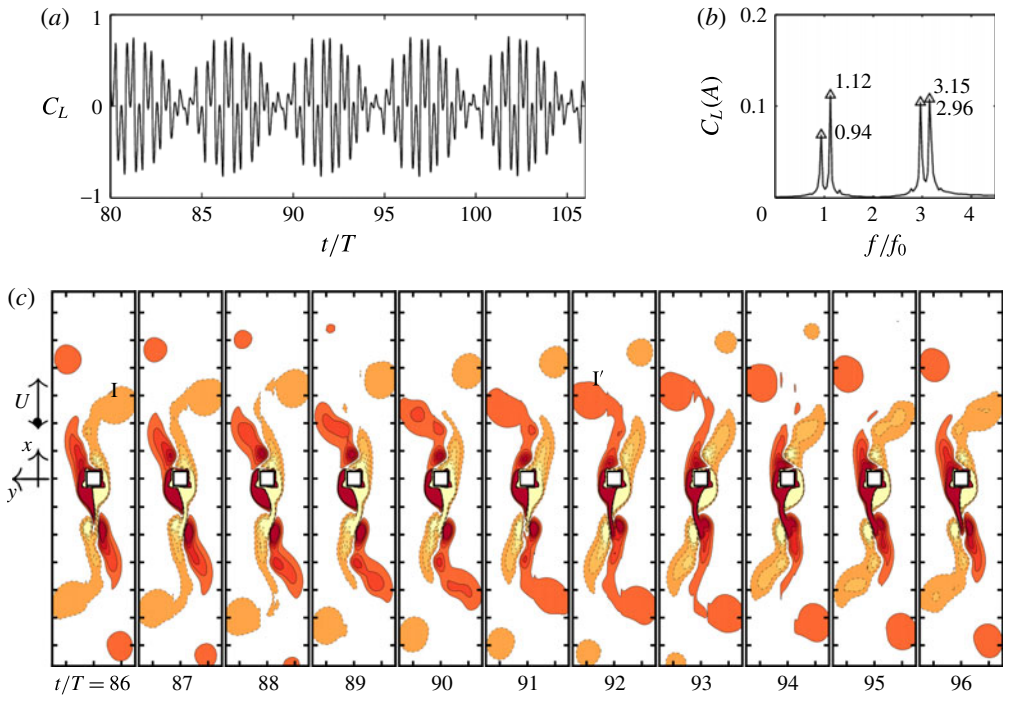

FIGURE 7. (Colour online) Characteristics of typical regime F′ at $(Re, KC) = (140, 11)$. (*a*) Time history of the lift coefficient; (*b*) fast Fourier transform (FFT) spectrum of the lift coefficient and (*c*) vorticity contour in 11 periods at the same phase instant of oscillation, when the inlet velocity is about to switch to upwards.

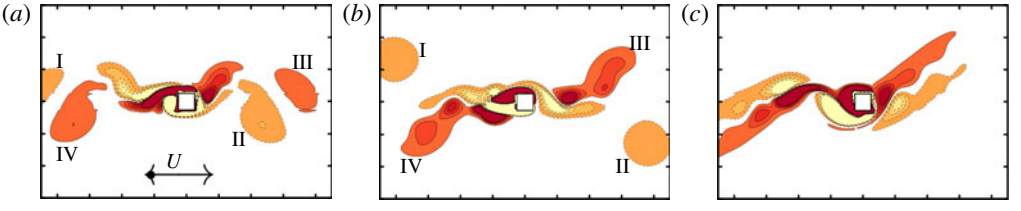

FIGURE 8. (Colour online) Instantaneous vorticity contour of (*a*) regime C at $(Re, KC) = (160, 7)$, (*b*) regime F′ at (140, 11.25) and (*c*) regime F at (100, 14).

frequency, similar to that in regime F′. It can also be seen that the generation processes of the Kármán vortex street at each side of the cylinder in regimes F′ and C are similar. The large vortex cores relatively far away from the body, as marked by I & II and III & IV in figure 8, are generated over multiple periods of oscillation and then shed alternately. Regime F′ and regime F are alike in the sense that the shed vortices are diagonally distributed.

It is believed due to the size of the secondary periods, regime F′ flows in figure 4 are visually distinct from one another. To examine the dependence of regime F′ flows on initial conditions, a DNS simulation was performed at $(Re, KC) = (140, 11)$ with an initial condition of the fully developed flow field obtained at (200, 12) in figure 4.

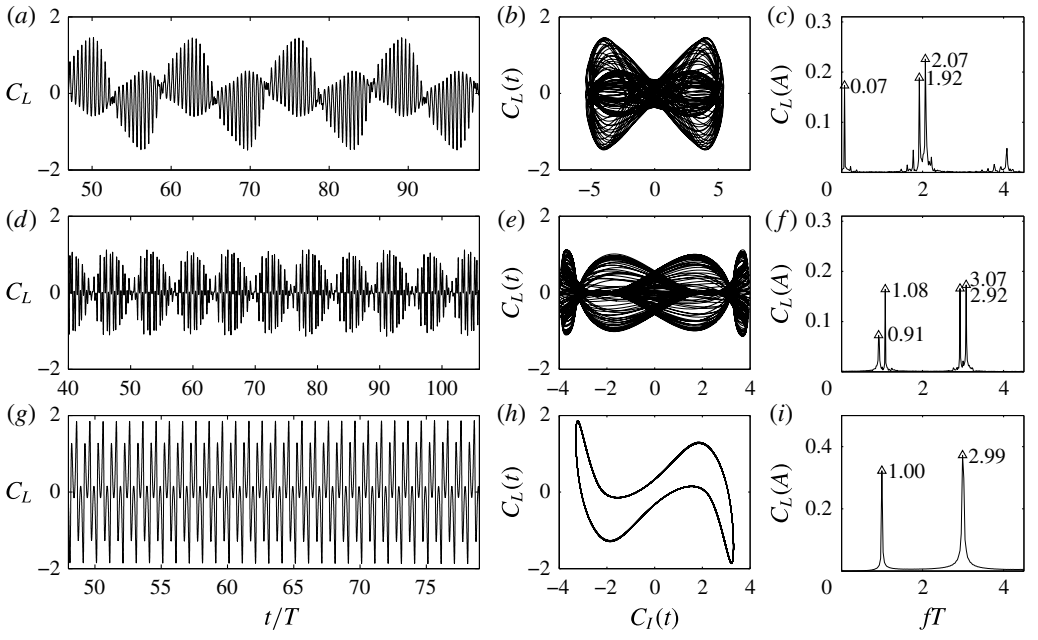

FIGURE 9. Comparison of the force behaviours of regime C, regime F′ and regime F, from top to bottom from the cases in figure 8. From left to right, columns are the time history of lift coefficient C_L (*a*,*d*,*g*), Lissajous plots of lift coefficient against in-line force coefficient C_l (*b*,*e*,*h*), and FFT spectra of the lift coefficient (*c*,*f*,*i*).

The result showed that the started regime G flow converted to regime F′ in less than 22 periods. This appears to suggest that regime F′ flows are not sensitive to initial conditions.

One further point worth mentioning in regime C and regime F′ is that although the combined vortex street at each side of the cylinder resembles a Kármán vortex street (Tatsuno & Bearman 1990; Elston *et al.* 2006), the frequency at which the vortex cores are shed can be different, which is different from that of the Kármán vortex. Figure 10 illustrates this point at $(Re, KC) = (140, 8)$. It is seen that C_L oscillates above the mean-zero value at approximately a period of $24T$, and this is the shedding frequency of the pair of vortices above the x-axis (similar to vortex I and III in figure 8*a*). However below the mean-zero level, C_L oscillates at approximately a period of $20T$, leading to a slightly lower shedding frequency for the pair of vortices below the x-axis (similar to vortex II and IV). This feature happens at the boundary of regime C, where the flow is about to transition to regime E.

3.2. *Outcome of stability analysis*

In order to capture the curve of marginal stability where the flow breaks 2-D K_y symmetry in (2.2), Floquet stability analysis was performed on oscillatory flow around the square cylinder. The base flow was obtained by solving the full nonlinear incompressible NS equations with similar boundary conditions to those in the DNS study, but since only 2-D symmetry-breaking instabilities are considered here, a symmetry boundary condition along $y = 0$ is enforced by computing over a half-domain, following the method reported by Elston, Sheridan & Blackburn (2004).

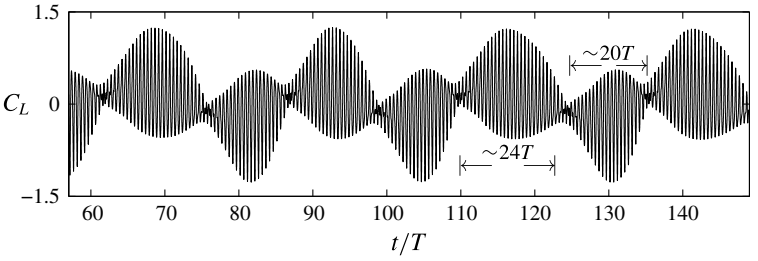

FIGURE 10. Frequency modulation as presented by the time history of the lift coefficient at $(Re, KC) = (140, 8)$.

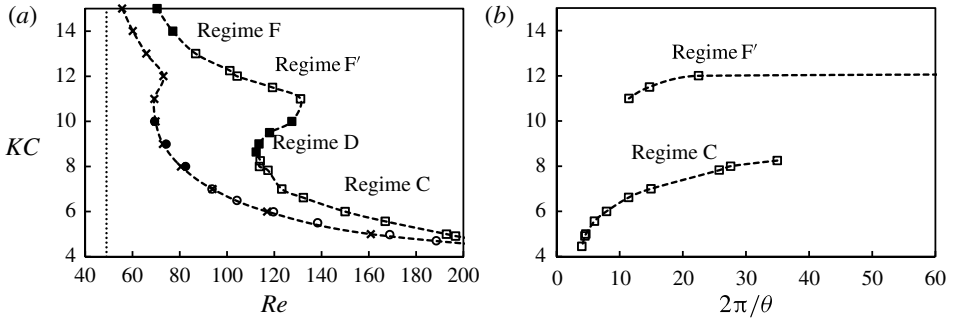

FIGURE 11. Outcomes of Floquet analysis for two-dimensional flows around a square and circular cylinder. (*a*) The curve of marginal stability for a square cylinder (□). The marginal curve for the circular cylinder from Elston *et al.* (2006) is included (○) for comparison, along with data from the present simulations (×). Filled symbols represent that real multipliers cross the unit circle at $|\mu| = 1$, while void symbols indicate the critical multipliers occur in complex-conjugate pairs (again with $|\mu| = 1$). A vertical dotted line shows the critical *Re* of the primary instability in unidirectional flow for both geometries (~49). (*b*) The phase angles of the multipliers as a function of *KC* for the square cylinder. Approximate locations of the identified flow regimes for the square cylinder are given in both (*a*) and (*b*).

When the simulation reaches the saturated state, a total of 64 flow-field slices are sampled, equispaced in time over the oscillating period T. These flow slices were used to generate the base flow over the whole domain. Stability analysis with the base flow was then performed by computing the linearised NS equations and seeking the leading eigenvalues with the Floquet solver embedded in Nektar++. A random vector field was used as the initial perturbation, with $\boldsymbol{u}'(x, y, t) = \boldsymbol{0}$ on all boundaries and a high-order Neumann boundary condition for perturbation pressure (Karniadakis, Israeli & Orszag 1991). The marginal stability is estimated by extrapolating the Floquet multiplier to 1, from the two cases in which the magnitudes of $\mu = \exp(\sigma T)$ are just above 1 (Elston *et al.* 2004).

The resultant curve of marginal stability has been included in figure 5 and is reproduced in figure 11(*a*) for clarity. The overall agreement between DNS and stability analysis suggests that when the enforced symmetry condition is removed, the flow breaks the reflection symmetry (2.2) into four different types of periodic and quasi-periodic modes. In particular, the flow breaks H_2 symmetry (2.4) in regime D at $8.25 < KC \leqslant 10$ and it breaks H_1 symmetry (2.3) in regime F for $KC \geqslant 14$.

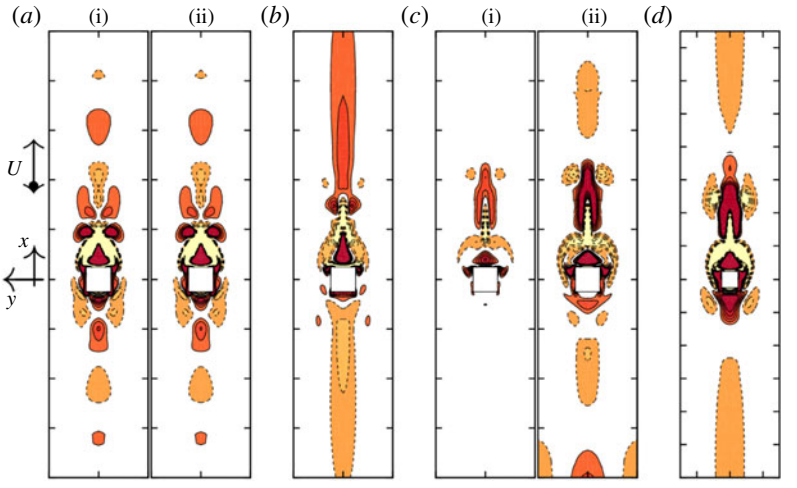

FIGURE 12. (Colour online) Vorticity contours of the Floquet eigenfunction for the four identified reflection symmetry-breaking regimes. (*a*) Regime C at $(Re, KC) = (150, 6)$ with $\mu = 1.0007\exp \pm \mathrm{i}0.7945$; (*b*) regime D at (116, 9) with $\mu = +1.039$; (*c*) regime F′ at (110, 12) with $\mu = 1.003\exp \pm \mathrm{i}0.2574$; (*d*) regime F at (78, 14) with $\mu = +1.043$. Both imaginary (i) and real part (ii) of the eigenfunction are given for the two QP regimes.

Staggered within these synchronous modes, the QP modes of regime C is observed at $4 < KC \leqslant 8.25$ and regime F′ at $11 \leqslant KC \leqslant 13$. It is seen whenever the flow breaks into QP states (regime C and F′) the critical multipliers are complex-conjugates, $\mu_c = \exp \pm \mathrm{i}\theta$; and whenever the flow breaks into synchronous states (regime D and F) the critical multiplier is real, $\mu_c = +1$. This demonstrates that the QP instability and the synchronous instability occur alternately for the square cylinder along the curve of marginal stability, extending on the findings of Elston *et al.* (2006).

For regime C and regime F′ a secondary period T_s appears along with a phase angle θ in the critical multipliers. The relationship $T_s/T = 2\pi/\theta$ observed by Elston *et al.* (2006) for a circular cylinder in 2-D simulations also holds for the square cylinder. The ratios of $2\pi/\theta$ along the marginal curve of stability are plotted as a function of KC in figure 11(*b*), where it shows that the secondary period increases with KC before the flow switches to a synchronised mode. It should be noted that an effort was also made in seeking regime F′ around a circular cylinder along the curve of marginal stability, especially around $KC = 11$, but no apparent characteristics of regime F′ flow were found.

It is interesting to see that the curve of marginal stability for the square cylinder stays to the right of the curve of the circular cylinder. Both marginal curves show strong inverse *Re*–*KC* relationships at low and high values of KC, except at intermediate KC. The shift is relatively small at either end of the KC range ($KC < 7$ and $KC > 13$), but is more significant for intermediate values of KC. This appears to suggest that the influence of structural geometry is weak at either small or large KC, but relatively strong at intermediate KC. The observation is perhaps not coincidental. At low Re but high KC the difference in geometry is overshadowed by viscous effects. In unidirectional flow (to which the marginal curves in figure 11 are expected to limit towards for large KC), for example, the locations of primary instability of a square cylinder (zero incidence) and a circular cylinder are close: i.e.

$Re = 47 \pm 2$ (Sohankar, Norberg & Davidson 1998) compared to $Re = 49$ (Williamson 1996). At low KC but high Re the whole shape of the geometry tends to be less significant due to the high frequency of oscillation. The shift in the curve for the square cylinder compared with the circular cylinder at intermediate KC and Re is discussed further in the next section.

The vorticity contours of the Floquet eigenfunction around criticality are shown in figure 12 for each of the identified flow regimes. It is seen that the leading eigenfunctions also occur in complex-conjugate pairs for the two QP modes, whereas they are real for the two synchronised modes. Depending on the phase angle of the critical multipliers, the size of the imaginary part can be almost equal to, or much smaller than, the real part (figure 12*a*,*c*). The vorticity contour seems to extend further in the two synchronised modes than that in the QP modes. The vorticity contours within regime C and D are, respectively, visually similar to that reported around a circular cylinder (Elston *et al.* 2006), which appears to suggest that the geometry difference brings limited influence to the contours of the critical eigenfunctions.

3.3. *Modulation between oscillation and vortex formation frequencies*

Since the vortex formation and shedding in oscillatory flow is heavily influenced by the oscillation period for the KC numbers considered, the intrinsic vortex-shedding feature in unidirectional flow is employed to explore the modulation between oscillation and vortex formation frequencies. For convenience we introduce KC_{St} to represent the non-dimensional vortex-shedding period due to steady flow, i.e. the reciprocal of St, to allow for comparison with KC in oscillatory flow. Thus,

$$KC_{St} = \frac{U_\infty}{f_{vs} D} = \frac{U_\infty T_{vs}}{D}, \tag{3.2}$$

where T_{vs} is the vortex-shedding period in unidirectional flow.

3.3.1. *Flow evolution at a fixed Re*

Numerical simulations at various KC cutting through $Re = 140$ were performed to demonstrate how the flow evolves with KC/KC_{St}, the oscillation period number to the vortex formation period in otherwise steady flow. Figure 13 presents FFT spectra associated with the time series of the lift coefficient for $6.25 \leqslant KC \leqslant 14$, along with instantaneous flow fields at selected KC numbers. The St at this selected Re is 0.153 (see figure 3), corresponding to $KC_{St} = 6.52$ and thus, KC/KC_{St} is in the range of 0.96–2.15.

For $KC \leqslant 6.25$ ($KC/KC_{St} < 0.96$) C_L is zero for $Re = 140$. The K_y symmetry (2.2) is maintained because during each half-cycle of movement, only a pair of vortices equal in size can generate, which are forced to detach from the cylinder by new vortices with opposite sign generated from near the body surface after the velocity reverses.

At $KC = 6.5$ ($KC/KC_{St} \approxeq 1$) the K_y symmetry (2.2) is broken in figure 13, where a low secondary frequency ($f_s/f_o \sim 0.10$) appears and modulates the major peaks so that a pair of peaks appear around $f/f_o = 2$ (and 4). This indicates the generation of the QP mode of regime C. The f_s/f_o then reduces as the KC increases beyond 6.5 so that the distance between the two peaks decreases. At about $KC = 9$, f_s/f_o decreases to almost zero, thus the two peaks combine into one, leading to the start of regime D. In this sense, regime D is a special case of regime C in which f_s/f_o approaches zero.

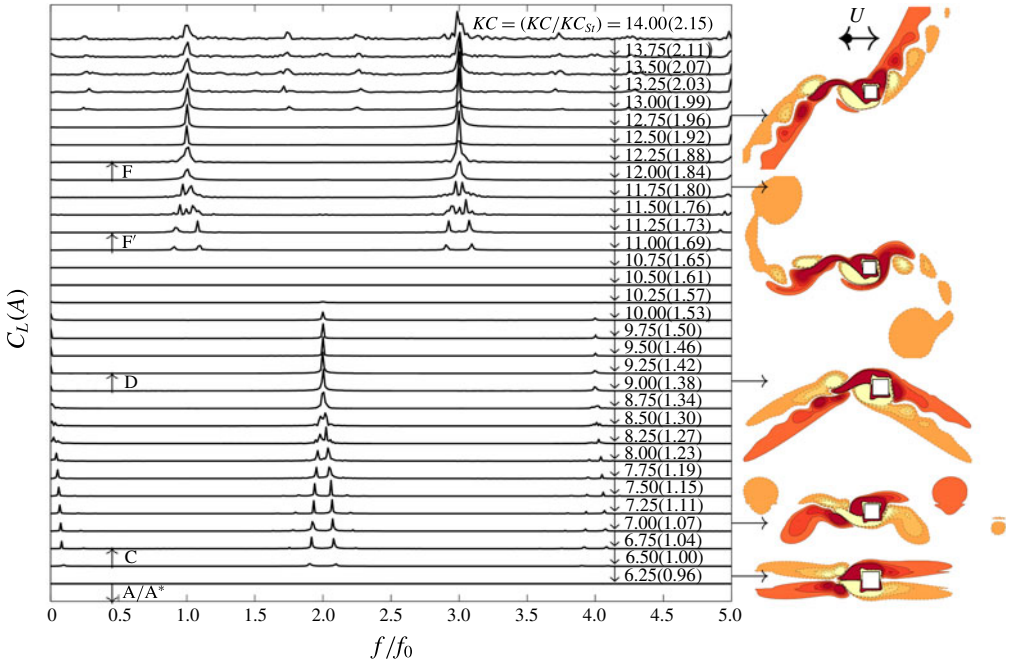

FIGURE 13. (Colour online) Characteristics of the flow regimes along $Re = 140$ and various KC (as labelled). Left, FFT spectra of the lift coefficient, where the frequency associated with the time series of the lift coefficient, f, is non-dimensionalised by oscillation frequency, $f_o = 1/T$, for each case. To facilitate comparison, spectra of FFT are translated in the vertical axis, where the amplitudes between any two neighbouring cases is 0.25. Same line at $KC = 11$ is presented in figure 7 and at $KC = 11.25$ in figure 9. Right, the flow field as illustrated by vorticity contour (from top to bottom at $KC = 12.75$, 11.75, 9, 7 and 6.25).

When KC is within the range 6.5–8.75 ($1 < KC/KC_{St} < 1.34$), as illustrated in figure 14, there is just enough time during each oscillation half-cycle to allow one pair of vortices (I and I′ at $t/T = 85$) to develop into different sizes, but not enough time to allow either of them to completely shed in the present half-cycle. Instead in the second half-cycle of oscillation, the pair of vortices move backwards and experience a very complicated process of vortex splitting, merging and shedding. Following this, at $t/T = 86$ a new vortex pair II and II′ replace I and I′, respectively. Because the majority of the vortices (which coincide with low pressure) are shed from the right-hand side of the cylinder over the time series shown in figure 14, the lift coefficient is mostly negative. Furthermore, because two major vortices are shed in one cycle, the period associated with the lift force is half of the oscillation period.

The consecutive development of vortex I′ and II′ after one cycle of oscillation is presented in figure 15. It is observed that the vortex slightly changes in size after each cycle and it is this difference which is believed to be responsible for modulating the shedding frequency. This difference is directly caused by the residual vortex I′ (or II′) being forced to circulate around the cylinder during one cycle of movement. As KC increases within the range 6.5–9 an increased portion of vortex I′ is shed in the half-cycle following its generation, which means the residual vortex I′, that modulates the flow field, decreases in strength and consequently the secondary period increases.

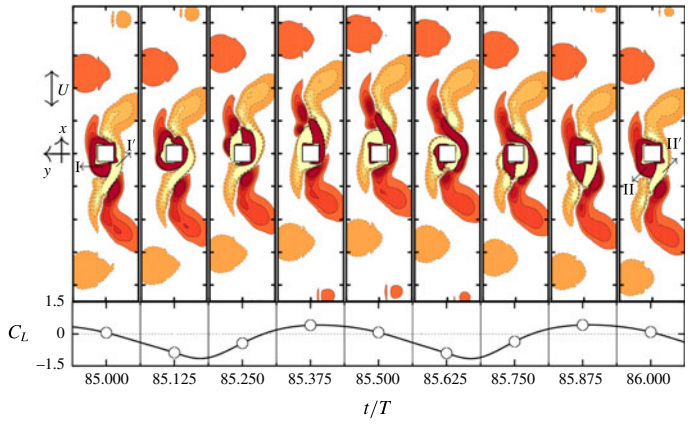

FIGURE 14. (Colour online) Detailed instantaneous flow fields and the lift coefficient in regime C at $(Re, KC) = (140, 7)$ in one selected oscillatory period, corresponding to that when the lift reaches minimum in the secondary period, as seen in the dashed box in the top plot in figure 15.

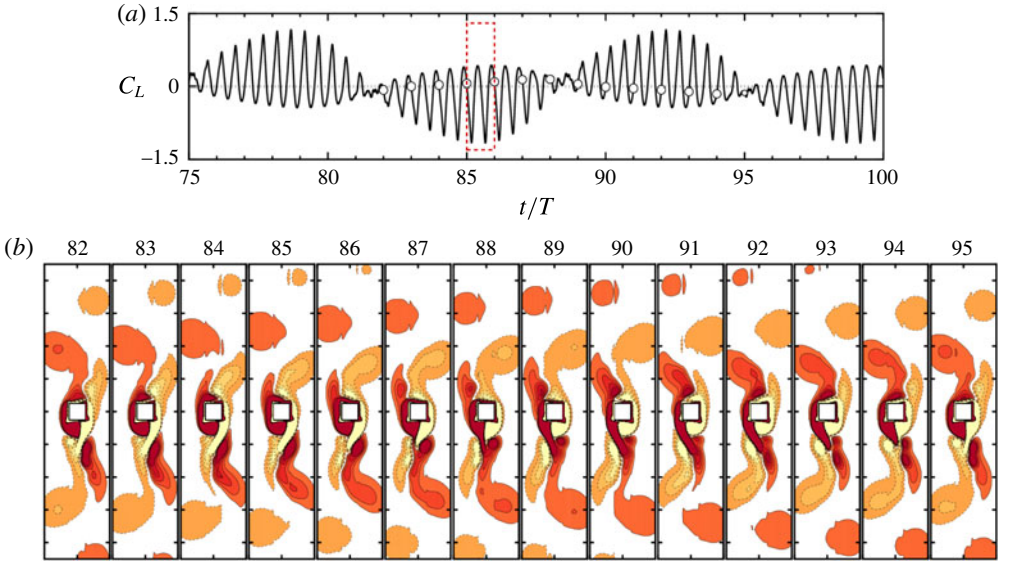

FIGURE 15. (Colour online) The evolution of regime C flow at $(Re, KC) = (140, 7)$. (*a*) Time history of lift coefficient; and (*b*) vorticity contour in 14 periods at selected time instants, corresponding to approximately a secondary period. The chosen instants are indicated by ○ in the graph of the lift coefficient.

When KC further increases from $KC = 9$, regime D takes over. During each half-cycle, there is enough time for a pair of different size vortices to be completely shed in the next half-cycle, despite complicated vortex splitting and mergence. Thus the flow field is exactly the same after one cycle of oscillation.

At $KC = 11$ ($KC/KC_{St} = 1.69$) a low frequency starts to modulate the major peaks again, leading to a pair of peaks at around $f/f_o = 1$ (and 3) in figure 13. This indicates

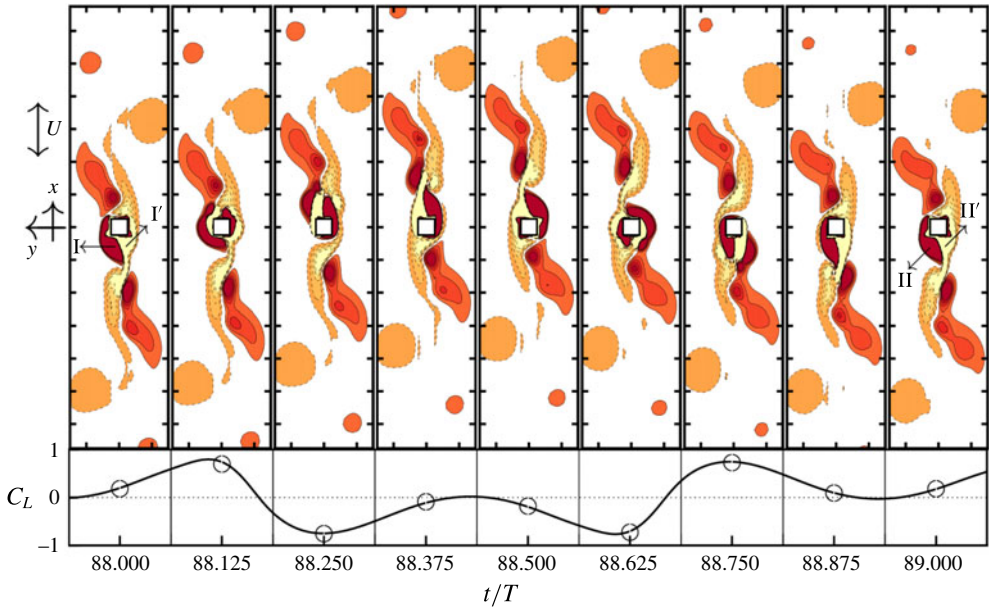

FIGURE 16. (Colour online) Detailed instantaneous flow fields and lift coefficient in regime F′ at $(Re, KC) = (140, 11)$ in a selected oscillatory period, as seen in figure 7, where the amplitude of lift reaches maximum.

the generation of another QP mode of regime F′. Again, f_s/f_o reduces with a further increase in KC, so that the distance between the two peaks reduces. At approximately $KC = 12$ at $Re = 140$ (slightly lower than $2KC_{St} = 13.04$), f_s/f_o decreases to a value close to zero and the two peaks combine into one. Physically, the reasons for the generation of regime F′ is similar to regime C. When KC is within the range 11–12, the time between flow reversals is not long enough to allow a pair of vortices to be completely shed from the cylinder, as illustrated in figure 16. Consequently the vortex residual (i.e. the part of the vortex forced to move back with in the second half-cycle) modulates the flow field during its accumulation in multiple cycles of oscillation. This reasoning is consistent with figures 14 and 15, which indicates that the QP flow phenomenon appears to be induced by the mismatch between the oscillation period and the time required for vortex formation. For $KC \geqslant 12$, the flow transitions to regime F. This is because that for each half-cycle of oscillation there is enough time for a pair of vortices to shed from the cylinder.

3.3.2. *Regime locations relative to KC_{St}*

Figure 17 illustrates the ratio of the secondary period to oscillatory period, T_s/T, at fixed KC and Re, respectively, highlighting the required number of cycles over which the flow tends to repeat itself. Here, T_s is derived from f_s in the FFT spectrum. The magnitude of T_s/T is believed to be related to the time difference between KC and KC_{St}, which determines how much vortex can be shed in one cycle of oscillation. Because the actual vortex formation in oscillatory flow is dependent on the oscillation frequency, a precise relationship for T_s as a function of KC and KC_{St} is not readily available. Despite that, T_s appears to change in agreement with the change of KC_{St}. Here at a constant KC, T_s/T roughly follows the same trend of St by comparing

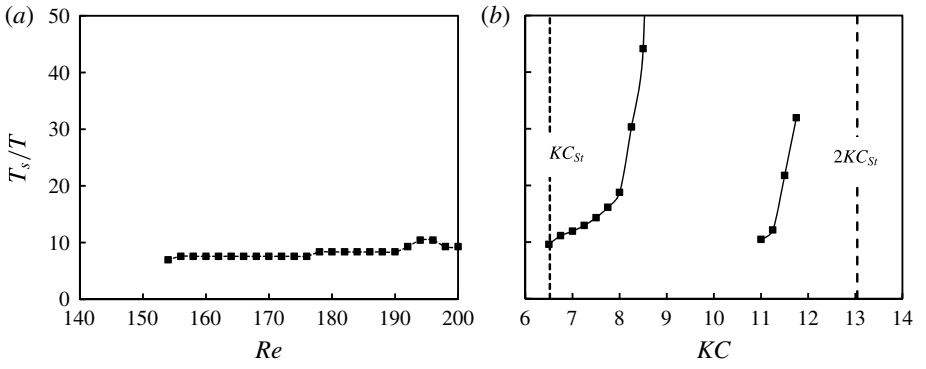

FIGURE 17. The dependence of the QP state on Re and KC as illustrated by the ratio of the secondary period (T_s) to the oscillation period (T) at (a) $KC = 6$ and (b) $Re = 140$.

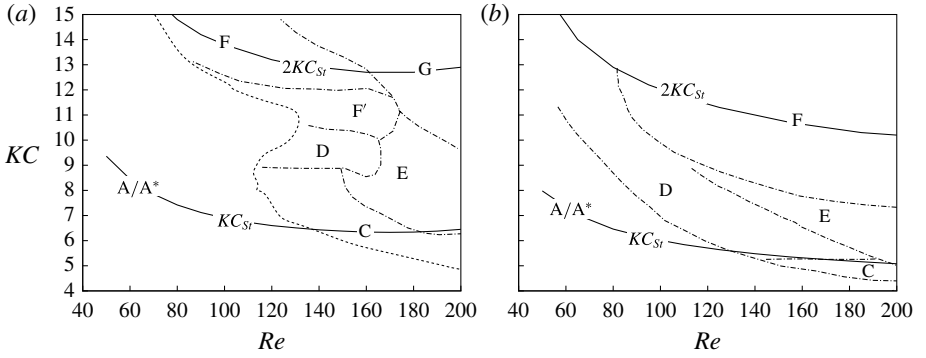

FIGURE 18. The relative locations of oscillatory flow regimes around a cylinder and the non-dimensional vortex-shedding period (KC_{St}) of the cylinder in the unidirectional flow. (a) Square cylinder; the regime boundaries are from figure 5 and solid lines of KC_{St} and $2KC_{St}$ are from figure 3. (b) Circular cylinder; the regime boundaries are from Tatsuno & Bearman (1990) and KC_{St} are from Williamson & Brown (1998) with $St = 0.2731 - 1.1129/\sqrt{Re} + 0.4821/Re$.

figures 17(a) and 3(a) for $Re = 140$–200. On the other hand at a constant Re, T_s/T becomes finite when KC is close to KC_{St} (or $2KC_{St}$).

Figure 18 presents a global view of all the flow regimes, and their relative locations in the parameter space compared to KC_{St} for both the square and circular cylinders, with the latter generated from published data. As discussed, the mechanism of the occurrence of two QP regimes C and F′ is thought to be related to the mismatch of oscillation period and the time required for vortex development and vortex shedding from the cylinder, which gives rise to the shedding of vortices in multiple cycles of oscillation. Although the vortex formation in oscillatory flow is highly influenced by KC, it is interesting that the two QP regimes locate close to the lines of KC_{St} or $2KC_{St}$, whereas regimes A, D and E fall mostly between the value of KC_{St} and $2KC_{St}$. The KC_{St} of the square cylinder is relatively larger than that of the circular cylinder for a given Re and it appears the flow regimes of the square cylinder shift upwards as a result. Furthermore, for intermediate values of KC number a lower Re is required for the flow around the circular cylinder to break K_y symmetry (2.2). Noting the shape

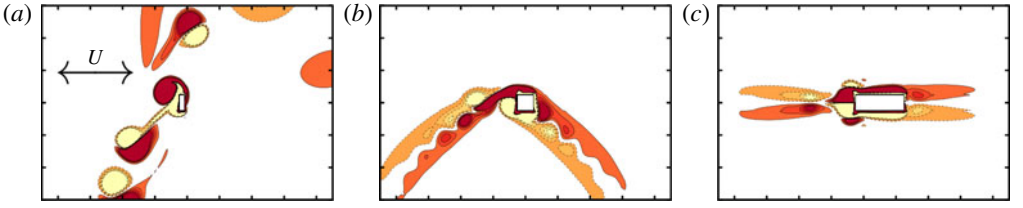

FIGURE 19. (Colour online) The dependence of flow regimes on the length (in the streamwise direction) of a rectangular cylinder, increasing from left to right at $(1/3)D$, D and $3D$, while the heights of the cylinders are kept at D. Flow fields are obtained through 2-D DNS simulations at $(Re, KC) = (160, 9)$.

Aspect ratio	1/3	2/3	1	3/2	3
St	0.1783	0.1667	0.1533	0.1517	0.1400
KC_{St}	5.61	6.00	6.52	6.59	7.14

TABLE 2. The non-dimensional vortex-shedding period (KC_{St}) of a rectangular cylinder with different aspect ratios placed in the uniform flow at $Re = 140$.

of the KC_{St} curves in figure 18 this is consistent with the fact that for a given KC number, $KC/KC_{St} \sim 1$ at a relatively smaller Re number for the circular cylinder, thus resulting in a leftwards shift in the flow regimes for the circular cylinder compared to the square cylinder.

3.3.3. *Flow dependence on St*

The shift of flow regimes as observed between square and circular cylinders is further explored by considering rectangular cylinders with different aspect ratios (where the aspect ratio is defined as the ratio of the width of cylinder in the flow direction to its height). A rectangular cylinder is chosen because its St is dependent on the configuration. It is therefore anticipated that a similar shift in flow regimes will be evident for rectangles with different aspect ratios. It should be noted that in the following discussion, Re, St and KC are all defined based on D, the facing height of the rectangular cylinder.

In the laminar regime for unidirectional flow, a reduction in St with an increase in aspect ratio was observed in the study of Okajima (1982) for a rectangular cylinder. This trend is consistent with the present DNS in table 2 at $Re = 140$. Based on these results and the understanding gained for the square cylinder, one would expect that the curves of marginal stability along with the flow regimes for a rectangular cylinder will shift to the right as the aspect ratio increases. This is because a general reduction in St across all Re implies that for intermediate KC number KC/KC_{St} becomes close to unit at a lower Re. This is confirmed through both DNS and Floquet stability analysis. Figure 19 illustrates the flow fields from DNS for a rectangular cylinder with aspect ratio of 1/3, 1 and 3 at $(Re, KC) = (160, 9)$, corresponding to flow characteristics of regime F, D and A, respectively.

The curves of the marginal stability for rectangular cylinders with aspect ratio of 2/3, 1 and 3/2 are shown in figure 20. It is observed that the marginal stability curve indeed moves towards the right as the aspect ratio increases. Similar dependence of flow regimes on aspect ratio was also observed in a recent work for elliptical foils

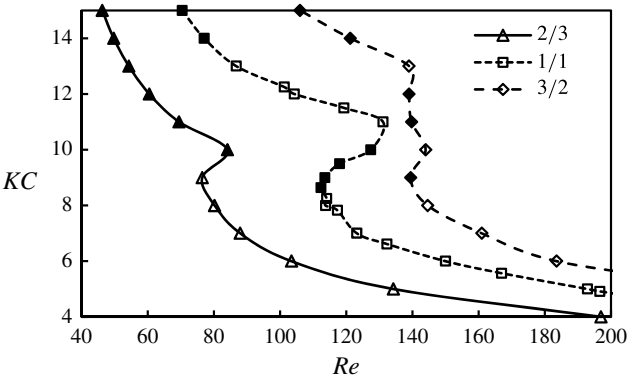

FIGURE 20. The dependence of the curve of marginal stability on the aspect ratios of a rectangular cylinder, increasing from left to right at 2/3, 1 and 3/2. Results were obtained from Floquet analysis.

in oscillatory flow, where the marginal stability curves move to a lower value of KC with the reduction of aspect ratio from 1 (circular cylinder) to 0.1 (see figure 5 in Deng & Caulfield 2016).

4. Conclusions

Flow regimes induced by oscillatory flow around a square cross-section cylinder at zero incidence angle were studied based on 2-D direct numerical simulations and Floquet stability analysis at intermediate Keulegan–Carpenter ($1 \leqslant KC \leqslant 15$) and low Reynolds ($Re \leqslant 200$) number. The main findings from the present study are summarised as follows:

(i) Compared with the family of flow regimes around a circular cylinder in oscillatory flow, two new flow regimes have been discovered for the square cylinder. One is characterised by the transverse convection of fluid particles at $KC \leqslant 2$ (regime A′), where the shear layers are forced to align with the leading edges of the square, causing the released particles to move perpendicular to the direction of flow oscillation. The second new flow regime is characterised by quasi-periodic flows at approximately $10 < KC < 13$ (regime F′), where the flow holds a well-defined secondary period, which is much larger than the oscillation period. The secondary period increases with the increase of KC until the flow synchronises again with the oscillation.

(ii) Moving along the curve of marginal stability, an alternate pattern in the modes of instability has been identified which break the reflection symmetry about the axis of motion. The instability is quasi-periodic at low KC, and becomes synchronous with the imposed oscillation between $8.25 < KC \leqslant 10$. The instability reverts to quasi-periodic with further increase in KC and becomes synchronous again above $KC = 13$. It is the second range of quasi-periodicity that leads to the newly observed flow regime F′.

(iii) The two quasi-periodic flow features appear to be induced by the mismatch between oscillation period and the time required for vortex formation and shedding. This has given rise to the incomplete shedding of a vortex core during one cycle of oscillation, whereas the residual vortex moves back with the

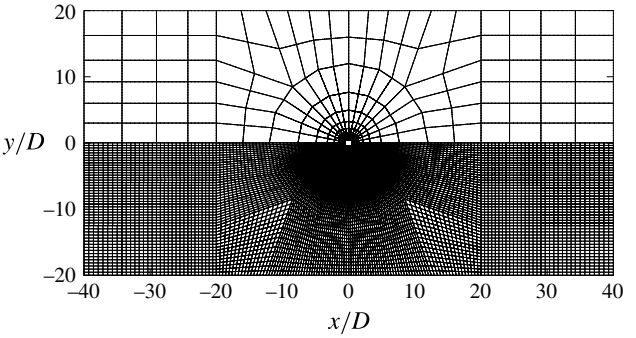

FIGURE 21. View of the domain and mesh used in the Floquet stability analysis. A domain size of $80D \times 40D$ with a total of 528 quadrilateral elements was chosen, adapted from meshes (*b*) and (*c*) in Elston *et al.* (2006). Each element shown in the top half of the domain contains N_p^2 mesh points, while in the bottom half, $N_p = 8$.

	$(Re, KC)\backslash N_p$ (total points)		$4(528 \times 4^2)$	$6(528 \times 6^2)$	$8(528 \times 8^2)$	$10(528 \times 10^2)$
(i)	(100, 8)	Peak C_I	5.2137	5.2012	5.1953	5.1937
		C_D	2.2525	2.2388	2.2329	2.2297
		C_M	2.0349	2.0301	2.0277	2.0270
(ii)	(200, 6)	Peak C_I	5.9998	6.0637	6.0536	6.0628
		C_D	2.1652	2.1609	2.1618	2.1481
		C_M	1.6306	1.6376	1.6284	1.6322
		R.m.s. C_L	0.6283	0.6098	0.6160	0.6287

TABLE 3. N_p-convergence results for the peak of in-line coefficients (C_I), drag and inertia coefficients (C_D and C_M) and the root-mean-square (r.m.s.) of the lift coefficients (C_L) of the square cylinder at (i) $(Re, KC) = (100, 8)$ and (ii) (200, 6). Only r.m.s. C_L at (ii) is given because the flow field of (i) is K_y symmetric.

reversed flow and accumulates in multiple cycles of motion. Compared to the non-dimensional vortex-shedding period in otherwise unidirectional flow (KC_{St}, the reciprocal of Strouhal number), the two quasi-periodic regimes locate close to the lines of KC_{St} or $2KC_{St}$. For oscillatory flow around a bluff body of different geometry from a circular cylinder, the marginal stability curve appears to shift in a way that is consistent with the shift of KC_{St} of the body from its circular counterpart, based on the results obtained with a limited number of rectangular geometries.

Acknowledgements

The input from three anonymous referees is greatly appreciated. This work was supported by resources provided by the Pawsey Supercomputing Centre with funding from the Australian Government and the Government of Western Australia.

Appendix

A mesh check was carried out for the Nektar++ (Cantwell *et al.* 2015) code before carrying out the Floquet stability analysis. A domain size of $80D \times 40D$

with 576 quadrilateral spectral elements was chosen based on the mesh checks from Elston *et al.* (2006). Figure 21 shows the computational domain and a typical mesh distribution, where the top half of the domain gives the distribution of the quadrilateral elements, while the bottom half illustrates the mesh points after eighth-order Lagrange polynomials expansion ($N_p = 8$). Here, the quadrilateral expansion was employed through the Gauss–Lobatto–Legendre quadrature points within each element. Table 3 provides a summary of the dependence study for a constant number of quadrilateral elements at two locations in the (Re, KC)-space. N_p from 4 to 10 were tested, resulting a global number of points ranging from 8448 to 52 800. The converged force coefficients in table 3 demonstrates that N_p effects are not significant for $N_p \geqslant 6$ and $N_p = 8$ is deemed to be sufficient.

REFERENCES

AN, H., CHENG, L. & ZHAO, M. 2011 Direct numerical simulation of oscillatory flow around a circular cylinder at low Keulegan–Carpenter number. *J. Fluid Mech.* **666**, 77–103.

BARKLEY, D. & HENDERSON, R. D. 1996 Three-dimensional Floquet stability analysis of the wake of a circular cylinder. *J. Fluid Mech.* **322**, 215–241.

BARRERO-GIL, A. 2011 Hydrodynamic in-line force coefficients of oscillating bluff cylinders (circular and square) at low Reynolds numbers. *J. Vib. Acoust.* **133** (5), 051012.

BEARMAN, P. W., DOWNIE, M. J., GRAHAM, J. M. R. & OBASAJU, E. D. 1985 Forces on cylinders in viscous oscillatory flow at low Keulegan–Carpenter numbers. *J. Fluid Mech.* **154**, 337–356.

BEARMAN, P. W., GRAHAM, J. M. R., OBASAJU, E. D. & DROSSOPOULOS, G. M. 1984 The influence of corner radius on the forces experienced by cylindrical bluff bodies in oscillatory flow. *Appl. Ocean Res.* **6** (2), 83–89.

CANTWELL, C. D., MOXEY, D., COMERFORD, A., BOLIS, A., ROCCO, G., MENGALDO, G., DE GRAZIA, D., YAKOVLEV, S., LOMBARD, J.-E., EKELSCHOT, D. *et al.* 2015 Nektar++: An open-source spectral/hp element framework. *Comput. Phys. Commun.* **192**, 205–219.

CHERN, M.-J., LU, Y.-J., CHANG, S.-C. & CHENG, I.-C. 2007 Interaction of oscillatory flows with a square cylinder. *J. Mech.* **23** (04), 445–450.

DENG, J. & CAULFIELD, C. P. 2016 Dependence on aspect ratio of symmetry breaking for oscillating foils: implications for flapping flight. *J. Fluid Mech.* **787**, 16–49.

ELSTON, J. R., BLACKBURN, H. M. & SHERIDAN, J. 2006 The primary and secondary instabilities of flow generated by an oscillating circular cylinder. *J. Fluid Mech.* **550**, 359–389.

ELSTON, J. R., SHERIDAN, J. & BLACKBURN, H. M. 2004 Two-dimensional Floquet stability analysis of the flow produced by an oscillating circular cylinder in quiescent fluid. *Eur. J. Mech. (B/Fluids)* **23** (1), 99–106.

GRAHAM, J. M. R. 1980 The forces on sharp-edged cylinders in oscillatory flow at low Keulegan–Carpenter numbers. *J. Fluid Mech.* **97** (02), 331–346.

HONJI, H. 1981 Streaked flow around an oscillating circular cylinder. *J. Fluid Mech.* **107**, 509–520.

JUSTESEN, P. 1991 A numerical study of oscillating flow around a circular cylinder. *J. Fluid Mech.* **222**, 157–196.

KARNIADAKIS, G. E., ISRAELI, M. & ORSZAG, S. A. 1991 High-order splitting methods for the incompressible Navier–Stokes equations. *J. Comput. Phys.* **97** (2), 414–443.

KEULEGAN, G. H. & CARPENTER, L. H. 1958 Forces on cylinders and plates in an oscillating fluid. *J. Res. Natl Bur. Stand.* **60** (5), 423–440.

KOEHLER, C., BERAN, P., VANELLA, M. & BALARAS, E. 2015 Flows produced by the combined oscillatory rotation and translation of a circular cylinder in a quiescent fluid. *J. Fluid Mech.* **764**, 148–170.

NEHARI, D., ARMENIO, V. & BALLIO, F. 2004 Three-dimensional analysis of the unidirectional oscillatory flow around a circular cylinder at low Keulegan–Carpenter and β numbers. *J. Fluid Mech.* **520**, 157–186.

OKAJIMA, A. 1982 Strouhal numbers of rectangular cylinders. *J. Fluid Mech.* **123**, 379–398.

SARPKAYA, T. 1976 Vortex shedding and resistance in harmonic flow about smooth and rough circular cylinders at high Reynolds numbers. *Tech. Rep.* NPS-59SL7602. Naval Postgraduate School, Monterey, CA.

SARPKAYA, T. 2002 Experiments on the stability of sinusoidal flow over a circular cylinder. *J. Fluid Mech.* **457**, 157–180.

SCOLAN, Y.-M. & FALTINSEN, O. M. 1994 Numerical studies of separated flow from bodies with sharp corners by the vortex in cell method. *J. Fluids Struct.* **8** (2), 201–230.

SMITH, P. A. & STANSBY, P. K. 1991 Viscous oscillatory flows around cylindrical bodies at low Keulegan–Carpenter numbers using the vortex method. *J. Fluids Struct.* **5** (4), 339–361.

SOHANKAR, A., NORBERG, C. & DAVIDSON, L. 1997 Numerical simulation of unsteady low-Reynolds number flow around rectangular cylinders at incidence. *J. Wind Engng Ind. Aerodyn.* **69**, 189–201.

SOHANKAR, A., NORBERG, C. & DAVIDSON, L. 1998 Low-Reynolds-number flow around a square cylinder at incidence: study of blockage, onset of vortex shedding and outlet boundary condition. *Intl J. Numer. Meth. Fluids* **26** (1), 39–56.

STOKES, G. G. 1851 On the effect of the internal friction of fluids on the motion of pendulums. *Trans. Camb. Phil. Soc.* **9**, 8–106.

TATSUNO, M. & BEARMAN, P. W. 1990 A visual study of the flow around an oscillating circular cylinder at low Keulegan–Carpenter numbers and low Stokes numbers. *J. Fluid Mech.* **211**, 157–182.

TONG, F., CHENG, L., ZHAO, M. & AN, H. 2015 Oscillatory flow regimes around four cylinders in a square arrangement under small *KC* and *Re* conditions. *J. Fluid Mech.* **769**, 298–336.

TROESCH, A. W. & KIM, S. K. 1991 Hydrodynamic forces acting on cylinders oscillating at small amplitudes. *J. Fluids Struct.* **5** (1), 113–126.

VENUGOPAL, V., VARYANI, K. S. & BARLTROP, N. D. 2006 Wave force coefficients for horizontally submerged rectangular cylinders. *Ocean Engng* **33** (11), 1669–1704.

WANG, C.-Y. 1968 On high-frequency oscillatory viscous flows. *J. Fluid Mech.* **32** (01), 55–68.

WILLIAMSON, C. H. K. 1985 Sinusoidal flow relative to circular cylinders. *J. Fluid Mech.* **155**, 141–174.

WILLIAMSON, C. H. K. 1996 Vortex dynamics in the cylinder wake. *Annu. Rev. Fluid. Mech.* **28** (1), 477–539.

WILLIAMSON, C. H. K. & BROWN, G. L. 1998 A series in $1/\sqrt{Re}$ to represent the Strouhal–Reynolds number relationship of the cylinder wake. *J. Fluids Struct.* **12** (8), 1073–1085.

ZHAO, M. & CHENG, L. 2014 Two-dimensional numerical study of vortex shedding regimes of oscillatory flow past two circular cylinders in side-by-side and tandem arrangements at low Reynolds numbers. *J. Fluid Mech.* **751**, 1–37.

ZHENG, W. & DALTON, C. 1999 Numerical prediction of force on rectangular cylinders in oscillating viscous flow. *J. Fluids Struct.* **13** (2), 225–249.